Calibration and Accuracy Assessment in a Direct Georeferencing System in UAS Photogrammetry

Gabrlik, Petr; La Cour-Harbo, Anders; Kalvodova, Petra; Zalud, Ludek; Janata, Premysl

Published in:
International Journal of Remote Sensing

DOI (link to publication from Publisher):
10.1080/01431161.2018.1434331

Publication date:
2018

Document Version
Accepted author manuscript, peer reviewed version

Citation for published version (APA):
Gabrlik, P., La Cour-Harbo, A., Kalvodova, P., Zalud, L., & Janata, P. (2018). Calibration and Accuracy Assessment in a Direct Georeferencing System in UAS Photogrammetry. *International Journal of Remote Sensing*, *39*(15-16), 4931-4959. https://doi.org/10.1080/01431161.2018.1434331

ARTICLE TEMPLATE

Calibration and Accuracy Assessment in a Direct Georeferencing System for UAS Photogrammetry

Petr Gabrlik[a][b], Anders la Cour-Harbo[c], Petra Kalvodova[a], Ludek Zalud[a][b] and Premysl Janata[d]

[a]CEITEC - Central European Institute of Technology, Brno University of Technology, Brno, Czech Republic; [b]Department of Control and Instrumentation, Faculty of Electrical Engineering and Communication, Brno University of Technology, Brno, Czech Republic; [c]Department of Electronic Systems, Technical Faculty of IT and Design, Aalborg University, Aalborg, Denmark; [d]Department of Forest Management and Applied Geoinformatics, Faculty of Forestry and Wood Technology, Mendel University in Brno, Brno, Czech Republic

ARTICLE HISTORY
Compiled February 9, 2018

ABSTRACT
Unmanned aerial systems (UAS) have already proven useful in fields and disciplines such as agriculture, forestry, or environmental mapping, and they have also found application during natural and nuclear disasters. In many cases, the environment is inaccessible or dangerous for a human being, meaning that the widely used technique of aerial imagery georeferencing via ground control points cannot be employed. The present paper introduces a custom-built multi-sensor system for direct georeferencing, a concept that enables georeferencing to be performed without an access to the mapping area and ensures centimetre-level object accuracy. The proposed system comprises leading navigation system technologies in the weight category of micro and light UASs. A highly accurate global navigation satellite system receiver integrating the real time kinematic technology supports an inertial navigation system where data from various sensors are fused. Special attention is paid to the time synchronisation of all sensors, and a method for the field calibration of the system is designed. The multi-sensor system is completely independent of the used UAS.

The authors also discuss the verification of the proposed system's performance on a real mission. To make the results credible, a high number of test points are used, with both the direct and the indirect georeferencing techniques subjected to comparison, together with different calibration methods. The achieved spatial object accuracy (about 4 cm RMSE) is sufficient for most applications.

KEYWORDS
Photogrammetry, UAS, UAV, unmanned aerial system, direct georeferencing, remote sensing, aerial photography, RTK, GNSS

1. Introduction

Unmanned aerial systems (UAS) have become an important part of aerial photogrammetry. Compared to manned aircraft, they bring substantial advantages, especially in terms of the operating costs. The devices allow fast and safe aerial data acquisition,

---

CONTACT Petr Gabrlik. Email: petr.gabrlik@ceitec.vutbr.cz. Address: Brno University of Technology, CEITEC - Central European Institute of Technology, Purkynova 656/123, 612 00, Brno, Czech Republic

which significantly reduces the long product cycle known from traditional photogrammetry utilizing manned aircraft. Conversely, their payload capability and endurance is limited, therefore UASs are suitable for mapping local areas only. The payload limitation leads to the use of consumer-grade sensors, which are usually smaller and lighter than survey-grade sensors and metric cameras but provide lower accuracy and parameter stability. This drawback is partly compensated for by the low flight altitude, which allows us to reach superior ground resolution.

Most photogrammetry missions performed by micro and light UASs (below 5 kg and 5–50 kg respectively according Arjomandi et al. (2006)) rely on ground control points (GCP). The method using ground points to facilitate aerial imagery georeferencing is called indirect georeferencing (IG). Combining an onboard consumer-grade camera and survey-grade positioning equipment for ground measurement allows us to reach the centimetre-level spatial accuracy of an orthophoto or digital elevation model (DEM). Barry and Coakley (2013) present the RMSE accuracy of 2.3 cm and 3.5 cm for the XY plane and Z axis, respectively, while using fixed-wing aircraft flying at 90 m above ground level (AGL). Similar results are presented in Panayotov (2015), where the indirect georeferencing was supported by real time kinematics (RTK) enabled global positioning system (GPS) onboard UASs. The results are not very reliable due to the small number of test points (TP). A credible outcome of indirect georeferencing is presented by Fazeli, Samadzadegan, and Dadrasjavan (2016), whose multi-rotor UAS flying at 120 m AGL reached the spatial accuracy of 1.7 cm and 2.9 cm RMSE for the XY plane and Z axis, respectively. The main disadvantage of IG approach consists in the need of ground measurement, a time-consuming and sometimes even infeasible technique.

In recent years, lightweight survey-grade global navigation satellite systems (GNSS) receivers and inertial navigation systems (INS) have become available on the market. Their use onboard UASs allows the direct georeferencing (DG) of aerial imagery, eliminating the need of GCPs. The technique is commonly supported by feature-based computer vision (CV) algorithms to ensure position and attitude refinement; however, the approach also places high demands on the calibration of the onboard sensor system, especially on the lever arm compensation and time synchronisation. The accurate direct georeferencing systems used in micro and light UASs are discussed within several recent papers. Thus, for example, Fazeli, Samadzadegan, and Dadrasjavan (2016) present the RMSE accuracy of 16.4 cm and 23.5 cm for the XY plane and Z axis, respectively; the values were achieved using a multi-rotor UAS equipped with a single-frequency RTK module flying at 120 m AGL, and the accuracy was determined using 32 TPs. The implementation of the differential GPS (DGPS) onboard a multi-rotor UAS is outlined by Turner, Lucieer, and Wallace (2014). In this case, the orthophoto accuracy of 11 cm (mean) was reached. The differential GNSS receiver was further employed by Lo et al. (2015); the approach enables carrier phase measurement, but the reached object accuracy is in the order of meters when flying at 100 m AGL. Contrariwise, the superior ground accuracy values of 0.9, 0.6, and 0.9 cm RMS for the X, Y, and Z axes, respectively, are presented in a relevant study by Eling et al. (2015). These results were obtained thanks to a dual-frequency dual-antenna RTK GPS receiver, precise camera synchronisation, and lever arm compensation. However, only a small number of test points (9) was used for the accuracy determination, and the flight altitude was lower than normal in UAS missions (20 m AGL).

Different aspects of DG in the context of lightweight UASs are discussed in multiple other papers. For example, relevant studies by Sakr, Lari, and El-Sheimy (2016) and Rehak, Mabillard, and Skaloud (2013) describe multi-sensor system design and performance testing; Pfeifer, Glira, and Briese (2012) focus on determining the exterior orientation accuracy; Lari and El-Sheimy (2015) address various challenges related to data collection and processing, as well as quality control; and Elsharkawy and Habib (2016) introduce an error analysis of DG systems. These and similar recent contributions suggest that GCP-free photogrammetry performed by lightweight UASs has a great potential in the future.

1.1. *Contribution of the research*

The problems common to the current implementations of DG systems in micro/light UASs encompass the use of low accuracy GNSS receivers; the lack of INS/IMU, important for lever arm compensation; the insufficient accuracy of time synchronisation; and unreliable ground accuracy determination. The research discussed herein aims to employ the state-of-the-art technology in navigation and camera systems in the weight category suitable for micro/light UASs, utilizing available commercial software to facilitate photogrammetric processing with a high degree of automation; such an approach allows us to achieve a superior object accuracy without using GCPs. Thus, a custom multi-sensor system for UASs, comprising all necessary hardware, was developed and tested previously (Gabrlik, Jelinek, and Janata (2016)). In this context, the present paper introduces a custom calibration process for the given system, including the field estimation of major parameters. To render the procedures and their results credible, special attention was paid to accuracy determination in order to verify and confirm the proposed solution. The designed system exploits todays technologies (digital imaging and processing, integrated sensors, and UAS systems in particular) to enable fully automated aerial photogrammetry.

The system was developed at CEITEC laboratories and embodies a part of the ATEROS (Autonomous Telepresence Robotic System) robotic system (Zalud et al. (2015), Kocmanova and Zalud (2015)) structured by the team of Prof. Ludek Zalud. ATEROS comprises mainly terrestrial mobile robots with autonomous functions used for exploration and environmental mapping (Jilek (2015)), but its applicability is significantly expanded through employing a UAS capable of accurate aerial mapping.

The paper is subdivided into three main portions. Section 2 describes the basic theory of georeferencing in photogrammetry and discusses the designed multi-sensor system, including the calibration, data acquisition and processing. Section 3 presents the accuracy of the direct georeferencing of aerial imagery, focusing especially on object accuracy. The results are then outlined in Section 4, where a comparison with existing realisations is proposed.

2. Methods

This section introduces the methods and equipment used in the research. Following an insight into the theory of georeferencing and calibration, the UAS and the custom-built multi-sensor system are presented. Attention is also paid to the data processing and aerial data acquisition.

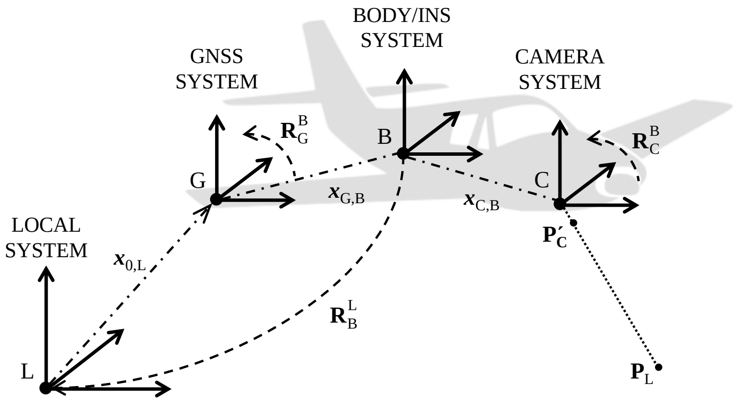

Figure 1. The relationship between the reference systems.

2.1. *Georeferencing in UAS photogrammetry*

Comparing the indirect and direct georeferencing techniques in UAS photogrammetry will not yield an unambiguous result, because each of the options exhibits certain advantages and disadvantages. The indirect approach, however, finds more frequent use, due in particular to less intensive requirements on the equipment carried by a UAS; further, the ground measurement of GCPs can be replaced by an existing georeferenced orthophoto when a high absolute accuracy is not needed. The DG technique places high demands on the system calibration, namely, the calibration of lever arms, angular misalignment of onboard sensors, and time synchronisation. Equation (1) describes the relationship between an image point $(\xi(t), \eta(t), -c)_{\mathrm{C}}^{\mathrm{T}}$ in camera system C, and an object point $(X(t), Y(t), Z(t))_{\mathrm{L}}^{\mathrm{T}}$ in local system L applied for DG. T letter in superscript is reserved for vector and matrix transposition; capital letters in vector subscript denote to a reference system; and in the case of rotation matrices, capital letters in subscript and superscript describe reference systems as follows: $\mathbf{R}_{\mathrm{from}}^{\mathrm{to}}$. Variable t always represents time.

$$\begin{aligned} \begin{bmatrix} X(t) \\ Y(t) \\ Z(t) \end{bmatrix}_{\mathrm{L}} &= \begin{bmatrix} X_0(t) \\ Y_0(t) \\ Z_0(t) \end{bmatrix}_{\mathrm{L}} + \mathbf{R}_{\mathrm{B}}^{\mathrm{L}}(\omega(t), \phi(t), \kappa(t)) \\ \left(\begin{bmatrix} X_{\mathrm{L}} \\ Y_{\mathrm{L}} \\ Z_{\mathrm{L}} \end{bmatrix}_{\mathrm{B}} \right. &+ \left. \lambda(\xi, \eta) \mathbf{R}_{\mathrm{C}}^{\mathrm{B}}(\Delta\omega, \Delta\phi, \Delta\kappa) \begin{bmatrix} \xi(t) \\ \eta(t) \\ -c \end{bmatrix}_{\mathrm{C}} \right) \end{aligned} \tag{1}$$

The formula comprises a spatial similarity transformation (Kraus (2007), Cramer (2001)) and a vector $(X_{\mathrm{L}}, Y_{\mathrm{L}}, Z_{\mathrm{L}})_{\mathrm{B}}^{\mathrm{T}}$ describing the distance (or lever arm) between the GNSS antenna and the camera perspective center in the body system B; another component of the formula consists in a rotation matrix, $\mathbf{R}_{\mathrm{C}}^{\mathrm{B}}$, characterizing the angular misalignment (or boresight angles) between the body and the camera system. These elements, together with the camera focal length c, are ideally constant. Vector $(X_0(t), Y_0(t), Z_0(t))_{\mathrm{L}}^{\mathrm{T}}$ expresses the position measured by the GNSS receiver in the local system, and rotation matrix $\mathbf{R}_{\mathrm{B}}^{\mathrm{L}}$ is obtained via INS measurement. By extension, the scale $\lambda(\xi, \eta)$ is not a constant either: it is individual for every image point.

In practice, an INS unit and a GNSS antenna are physically located at different

Table 1. The table of parameters calibrated in this paper.

Parameter	**Number of param.**	**Note**
Lever arm (translation vector)	3	Pre-calibrated, custom field calibration
Boresight angles	3	Pre-calibrated, *not used*
Synchronisation delay	1	Custom field calibration
Camera interior parameters	Up to 13	Pre-calibrated, field calibrated

places; thus, we introduce two different reference systems, namely, body B and GNSS G. Their mutual relationship is illustrated in Figure 1.

Once the 6 parameters defining the position and attitude of a camera – often referred to as camera exterior orientation or extrinsic parameters – are known, the position of an object point can be reconstructed if the object point is visible in at least two overlapped images. Subsequently, we get a pair of equations (2) for each of the images, and these formulae are solvable as they form a system of four equations with three unknowns $(X, Y, Z)_{\mathrm{L}}^{\mathrm{T}}$, namely, the object position. The elements r_{ij} in (2) represent the components of the rotation matrix transforming point from the camera system into the local system, where i represents row index and j column index. If, however, the object point is visible on a single image only, the Z coordinate cannot be reconstructed, because there are infinitely many solutions. The equations (2), often called collinearity equations, are typically solved using least square estimation. If aerial photographs exhibit large forward and side overlaps (Section 2.7), a highly over-determined system of equations can be used to estimate other unknowns, including camera interior parameters.

$$\begin{aligned} X &= X_0 + (Z - Z_0)\frac{r_{11}\xi + r_{12}\eta + r_{13}c}{r_{31}\xi + r_{32}\eta + r_{33}c} \\ Y &= Y_0 + (Z - Z_0)\frac{r_{21}\xi + r_{22}\eta + r_{23}c}{r_{31}\xi + r_{32}\eta + r_{33}c} \end{aligned} \tag{2}$$

2.2. *System calibration*

As mentioned in the previous section, direct georeferencing requires calibration. In our research, several calibration techniques (Table 1) are used to facilitate accurate object point determination. This subsection then introduces a custom system calibration procedure designed to estimate the constant parameters directly related to the DG accuracy, namely, the lever arm offset, base station offset, and synchronisation delay. The estimation of the parameters is not implemented in common photogrammetric software tools, because complex data are needed for the processing. The difference between a position measured by a GNSS receiver (transformed into a camera perspective centre using initial lever arm calibration) and the true position of an image comprises the aforementioned elements:

- Offset in the body B system (lever arm – 3D vector).
- Offset in the local L system (base station position error – 3D vector).
- Offset caused by a delay between the moment of capturing the image and that of storing the data (synchronisation delay – scalar).

The lever arm $\boldsymbol{x}_{\mathrm{lv,B}} = (X_{\mathrm{L}}, Y_{\mathrm{L}}, Z_{\mathrm{L}})_{\mathrm{B}}^{\mathrm{T}}$ outlined in equation (1) can be split into two main parts (3): the distance $\boldsymbol{x}_{\mathrm{g,B}} = (X_{\mathrm{G}}, Y_{\mathrm{G}}, Z_{\mathrm{G}})_{\mathrm{B}}^{\mathrm{T}}$ between the GNSS antenna and

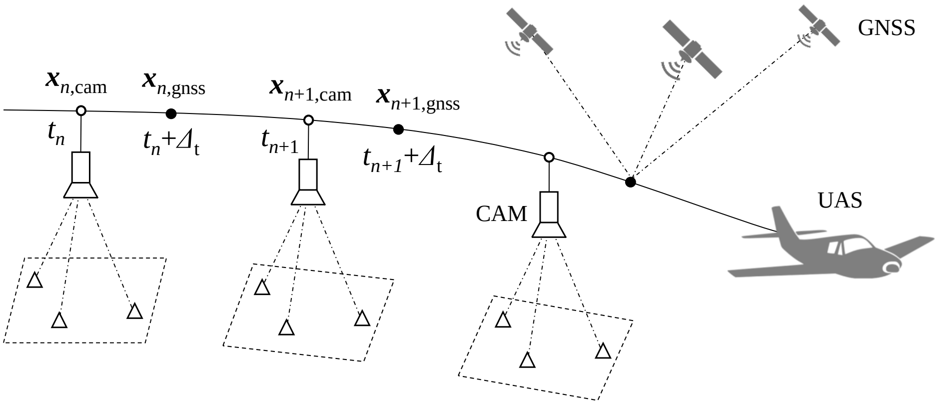

Figure 2. The difference between the AT-estimated image position $\boldsymbol{x}_{n,cam}$ and the GNSS/INS derived image position $\boldsymbol{x}_{n,gnss}$ is caused mainly by the lever arm and synchronisation delay Δ_t.

the INS unit, and the distance $\boldsymbol{x}_{\mathrm{c,B}} = (X_\mathrm{C}, Y_\mathrm{C}, Z_\mathrm{C})^\mathrm{T}_\mathrm{B}$ between the INS unit and the camera perspective centre (Figure 1). These two vectors are pre-calibrated (laboratory-estimated) before a flight and saved into the INS unit; the measured GNSS position is thus transformed to the camera perspective centre in real time. The total lever arm is then refined by the vector $\boldsymbol{\Delta}_{\mathrm{lv,B}} = (\Delta_\mathrm{lvx}, \Delta_\mathrm{lvy}, \Delta_\mathrm{lvz})^\mathrm{T}_\mathrm{B}$ obtained through the custom calibration.

$$\boldsymbol{x}_{\mathrm{lv,B}} = \boldsymbol{x}_{\mathrm{g,B}} + \boldsymbol{x}_{\mathrm{c,B}} + \boldsymbol{\Delta}_{\mathrm{lv,B}} \tag{3}$$

The boresight angles, similarly to the lever arm, can be pre-calibrated before a flight and then re-calibrated during the field calibration. Our research involved using the Agisoft Photoscan Professional photogrammetric software, which implements CV-based algorithms; further, the attitude of the aerial images (photogrammetric angles) is also estimable during the alignment stage, and the boresight angles thus need not be calibrated for the actual processing.

The base station offset $\boldsymbol{\Delta}_{0,\mathrm{L}} = (\Delta_\mathrm{0x}, \Delta_\mathrm{0y}, \Delta_\mathrm{0z})^\mathrm{T}_\mathrm{L}$ is the position error of the terrestrial GNSS receiver providing correction data for the onboard GNSS receiver. This inaccuracy then causes error in the multi-sensor system position measurement within the local reference system L. Since the offset remains constant during a mission, it can be estimated using the proposed calibration; however, the offset is specific for each base station, and thus it is not a calibration parameter of our system (contrary to the lever arm, which does not change).

The last estimated parameter lies in the synchronisation delay Δ_t between the camera shutter and GNSS/INS data logging. The error vector caused by this delay depends on not only the delay size but also the flight speed and direction (course). Since both the speed and the course are measured by the INS, the delay is estimable, as are the lever arm and base station offset. Based on the technical realisation, the delay can be positive or negative.

The problem consists in that the true (reference) position of the images is normally unavailable. For this purpose, indirect imagery georeferencing is applicable; the process is also known as aerial triangulation (AT). It can be argued that the procedure does not yield reference data, because the result is obtained through least-square estimation. However, with a large number of images taken in a suitable arrangement, and assuming multiple tie points and accurately measured ground control points, the estimated exterior orientation can be considered credible. Figure 2 illustrates the difference between the true image position (obtained via AT) and the measured image position (GNSS/INS-derived); the discrepancy arises predominantly from the aforementioned parameters. The GNSS and AT data are compared in Section 3.2.

$$\boldsymbol{x}_{\mathrm{e,L}} - \boldsymbol{x}_{\mathrm{m,L}} = \boldsymbol{\varDelta}_{\mathrm{0,L}} + \mathbf{R}_{\mathrm{B}}^{\mathrm{L}} \boldsymbol{\varDelta}_{\mathrm{lv,B}} + \mathbf{R}_{\mathrm{v}} \boldsymbol{v}_{\mathrm{B}} \varDelta_{\mathrm{t}} \tag{4}$$

Equation (4) represents the observation equation for the custom calibration to be assembled for every image. The difference between the estimated $\boldsymbol{x}_{\mathrm{e,L}} = (x_{\mathrm{e}}, y_{\mathrm{e}}, z_{\mathrm{e}})_{\mathrm{L}}^{\mathrm{T}}$ and measured $\boldsymbol{x}_{\mathrm{m,L}} = (x_{\mathrm{m}}, y_{\mathrm{m}}, z_{\mathrm{m}})_{\mathrm{L}}^{\mathrm{T}}$ image positions on the left-hand side is minimised by the unknowns $\boldsymbol{\varDelta}_{\mathrm{0,L}}$ (base station offset), $\boldsymbol{\varDelta}_{\mathrm{lv,B}}$ (lever arm offset), and $\varDelta_{\mathrm{t}}$ (synchronisation delay). The rotation matrix $\mathbf{R}_{\mathrm{B}}^{\mathrm{L}}$ transforms the lever arm vector from the body B to the local system L, and $\mathbf{R}_{\mathrm{v}}$ rotates the speed vector $\boldsymbol{v}_{\mathrm{B}} = (v_{\mathrm{x}}, v_{\mathrm{y}}, v_{\mathrm{z}})_{\mathrm{B}}^{\mathrm{T}}$ to the local system L. If the issue is solved in 3D, we obtain three equations (5) based on (4) for every image; this may mean hundreds of equations per calibration flight (N denotes the number of images). By contrast, there are 7 unknown parameters only (overlined). The elements p_{ij} and q_{ij} represent the components of the rotation matrices $\mathbf{R}_{\mathrm{B}}^{\mathrm{L}}$ and $\mathbf{R}_{\mathrm{v}}$ respectively, where i symbolises row index and j column index.

$$\begin{aligned}
x_{\mathrm{e}i} - x_{\mathrm{m}i} &= \overline{\varDelta}_{\mathrm{0x}} + p_{11i}\overline{\varDelta}_{\mathrm{lvx}} + p_{12i}\overline{\varDelta}_{\mathrm{lvy}} + p_{13i}\overline{\varDelta}_{\mathrm{lvz}} + (q_{11i}v_{\mathrm{x}i} + q_{12i}v_{\mathrm{y}i} + q_{13i}v_{\mathrm{z}i})\overline{\varDelta}_{\mathrm{t}} \\
y_{\mathrm{e}i} - y_{\mathrm{m}i} &= \overline{\varDelta}_{\mathrm{0y}} + p_{21i}\overline{\varDelta}_{\mathrm{lvx}} + p_{22i}\overline{\varDelta}_{\mathrm{lvy}} + p_{23i}\overline{\varDelta}_{\mathrm{lvz}} + (q_{21i}v_{\mathrm{x}i} + q_{22i}v_{\mathrm{y}i} + q_{23i}v_{\mathrm{z}i})\overline{\varDelta}_{\mathrm{t}} \\
z_{\mathrm{e}i} - z_{\mathrm{m}i} &= \overline{\varDelta}_{\mathrm{0z}} + p_{31i}\overline{\varDelta}_{\mathrm{lvx}} + p_{32i}\overline{\varDelta}_{\mathrm{lvy}} + p_{33i}\overline{\varDelta}_{\mathrm{lvz}} + (q_{31i}v_{\mathrm{x}i} + q_{32i}v_{\mathrm{y}i} + q_{33i}v_{\mathrm{z}i})\overline{\varDelta}_{\mathrm{t}} \\
&\qquad\qquad\qquad\qquad\qquad\qquad\qquad\qquad\qquad\qquad i = 1, 2, 3 \ldots N
\end{aligned} \tag{5}$$

The over-determined system of equations is then solved using the Gauss-Newton iterative method (Deuflhard (2011)). The vector of residuals $\boldsymbol{r}$ comprises the set of equations (5) $\boldsymbol{r} = \boldsymbol{f}(\varDelta_{\mathrm{0x}}, \varDelta_{\mathrm{0y}}, \varDelta_{\mathrm{0z}}, \varDelta_{\mathrm{lvx}}, \varDelta_{\mathrm{lvy}}, \varDelta_{\mathrm{lvz}}, \varDelta_{\mathrm{t}})$, and $\boldsymbol{\theta}$ represents the vector of the 7 calibration parameters, which is initialised by an initial approximation $\boldsymbol{\theta}_0$. This vector is updated in each iteration step k of the Gauss-Newton algorithm (6). $\mathbf{J}_{\mathrm{r}}$ stands for the Jacobian matrix, namely, the matrix of the first-order partial derivatives of $\boldsymbol{r}$.

$$\boldsymbol{\theta}_{k+1} = \boldsymbol{\theta}_k - (\mathbf{J}_{\mathrm{r}}^{\intercal}\mathbf{J}_{\mathrm{r}})^{-1}\mathbf{J}_{\mathrm{r}}^{\intercal}\boldsymbol{r}(\boldsymbol{\theta}_k), \tag{6}$$

The iteration ends once the given convergence conditions have been satisfied, typically when the difference $\boldsymbol{\theta}_{k+1} - \boldsymbol{\theta}_k$ is smaller than the value given for each unknown variable. The above-described calibration was implemented in Matlab and can be employed to estimate the unknown parameters in any calibration flight. However, two datasets are required: the reference image positions (AT-estimated in Photoscan within this research) and the GNSS/INS-derived data for every image, including the position, attitude, course, and speed.

The calibration parameters of the multi-sensor system, namely, the lever arm vector and the synchronisation delay, are applied to refine the measured position of every image, utilising another Matlab script (section 2.8); the data can be then used for the direct georeferencing. The outcomes of the custom calibration are presented in the

Section 3.

2.3. *Camera calibration*

Camera interior orientation (also intrinsic parameters) embodies a set of parameters characterizing the mechanical arrangement of the elements of a camera and a lens. A camera model based on central projection (equations (1), (2)) typically comprises the following linear parameters: focal length (c); principal point offset (ξ_0, η_0); and affinity and non-orthogonality coefficients (b_1, b_2) (Hartley and Zisserman (2004)). Based on Brown's model (Brown (1966), Brown (1971)), the distortion of a lens is described by radial (k_1–k_4) and tangential (p_1–p_4) non-linear parameters. The camera model applied in this paper is outlined in Agisoft (2017).

Although there are many camera calibration techniques, this paper aims to employ only two of the approaches most common in UAS photogrammetry. The former is pre-calibration using a checker board; we performed this step with Agisoft Lens. The software estimates the parameters via a pattern on the computer screen, whereas the photographs are captured from a close distance with different poses and positions. A disadvantage is that the focus setting varies from a real photogrammetry mission, and thus the intrinsic parameters can differ slightly.

The latter method rests in field (also on-site, on-the-job) calibration, where the camera interior orientation is estimated using actual project images, or real aerial data processed via Agisoft Photoscan in the described case. Advantageously, the desired actual camera parameters are estimated; however, we must also satisfy several conditions to obtain accurate results. Thus, for example, large overlaps should be present to locate points on many images, and the camera should cover a wide range of angles. If such conditions are met, the field calibration is more accurate than the pre-calibration; conversely, multiple photogrammetry projects comprise nadir photographs arranged in strips and blocks, which produce improper estimation conditions. These aspects are outlined by Harwin, Lucieer, and Osborn (2015) and Han, Park, and Lee (2016).

Both of the aforementioned approaches, namely, checker board pre-calibration and field calibration, are tested, and the performance is assessed using the object accuracy within Section 3.4.

2.4. *Multi-sensor system*

Besides the digital camera, the direct georeferencing technique in photogrammetry requires several other sensors and equipment onboard a UAS. Being the subject of a previous research, the development of the multi-sensor and logging system was published within Gabrlik, Jelinek, and Janata (2016).

To facilitate accurate position measurement, a Trimble BD982 GNSS receiver was used. This receiver supports the RTK technique to enhance the accuracy to centimetre-level, and a dual antenna input allows true heading measurement; the applied antennas are located 1.2 meters apart. The correction data for the receiver are obtained from a custom base station in real time. The base station comprises a 2.4 GHz wireless unit and another Trimble BD982 GNSS receiver configured to generate the correction data. The station has to be placed on a point with a known position to ensure absolute measurement accuracy (Section 2.6).

The attitude is measured using an SBG Ellipse-E INS unit, which integrates inertial sensors and fuses their data with external aiding data in an extended Kalman filter.

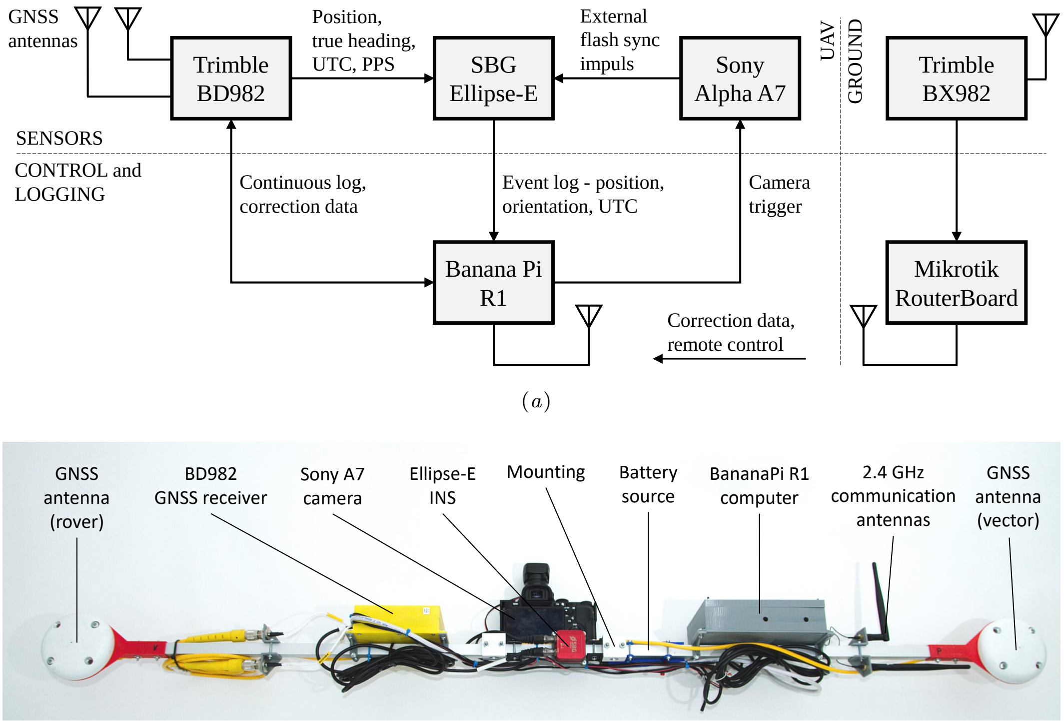

(a)

(b)

Figure 3. The custom-built multi-sensor system for the direct georeferencing.

The aiding data from the Trimble receiver provide an absolute position and heading reference with the frequency of 50 Hz; the fused navigation data are computed at 200 Hz. The INS also integrates the lever arm compensation between the GNSS antenna and the INS and between the INS and the camera sensor.

The multi-sensor system presented in the above-mentioned paper contained a Canon PowerShot G16 digital camera, later replaced with a Sony Alpha A7 camera having a Voigtlander lens to ensure better stability of the lens parameters and a higher image quality. The new camera is equipped with a full-frame sensor providing the resolution of 6,000 × 4,000 px and a 15 mm / F 4.5 fixed lens suitable for the pre-calibration. More parameters are presented in Table 2.

An essential part of a direct georeferencing system for UASs is embodied in the accurate time synchronisation of all sensors. The GNSS receiver and the INS are synchronised using a pulse per second (PPS) signal and NMEA messages containing UTC time. Unfortunately, most common consumer-grade cameras are not equipped with a synchronisation interface, and therefore a hot shoe adapter was used for the given purpose. Once an image has been taken, the signal for the external flash is used as the event signal for the INS, which then saves the current position, attitude, and other data. This approach has already been successfully employed in other similar projects, for example, that completed by Turner, Lucieer, and Wallace (2014). Despite the fact, a delay still exists between the actual image capturing and data storage; thus, the calibration and refinement of the measured data are needed (Section 2.2).

The data from the GNSS receiver and the INS are stored on the SSD storage of an onboard Linux computer BananaPi R1, which also finds application in triggering the camera at specific time intervals. The image data are stored on the SD card of the camera. The described multi-sensor system is shown in Figures 3(a) and 3(b).

Figure 4. The DJI S800 UAS equipped with the custom-built multi-sensor system.

Table 2. The parameters of the custom-built multi-sensor system.

Parameter	**Value**
Position accuracy (BD982)[a]	Horizontal: 8 mm, vertical: 15 mm
Attitude accuracy (Ellipse-E)[b]	Roll/pitch: 0.1°, heading: 0.4°
Camera resolution	6,000 × 4,000 px
Camera lens	15 mm / F 4.5
Operational time	120 mins
Distance from base	1,000 m
Dimensions	1.5 × 0.2 × 0.2 m
Weight	2.6 kg

[a] 1σ error in the RTK mode, according to the manufacturer's specification.

[b] The RTK mode in the airborne applications, according to the manufacturer's specification.

2.5. *UAS platform*

To test the multi-sensor system, we used a DJI S800 UAS (Figure 4), an 80 cm span hexacopter capable of flying for approximately 10 minutes with the payload of 2-3 kg. The UAS is fitted with a Wookong M flight controller to support automatic flight based on selected waypoints; for this reason, the device contains a low-accurate GPS receiver. The whole multi-sensor system can be easily mounted on the UAS without modifying its structure. The UAS and the multi-sensor system are completely independent of each other, mainly thanks to having autonomous power sources and communication interfaces.

The hoverability and high payload capacity are the central reasons why multi-rotor UASs are often employed in photogrammetry missions similar to that outlined herein (Rieke et al. (2012), Eling et al. (2015), Turner, Lucieer, and Wallace (2014)).

2.6. *Test area and ground measurement*

The test mission took place at the campus of Brno University of Technology, Brno, Czech Republic (49°13'41.61"N, 16°34'19.002"E — WGS84, Figure 5). The relevant area occupies almost 20,000 m^2 of grassy terrain with large height differences, multiple paths, and artificial objects. The locality meets the requirements for the operation of UASs, including the horizontal distance from buildings and urbanised zones.

The test area comprised 30 systematically distributed ground targets usable as ground control points (GCP) for imagery georeferencing or as test points (TP) to

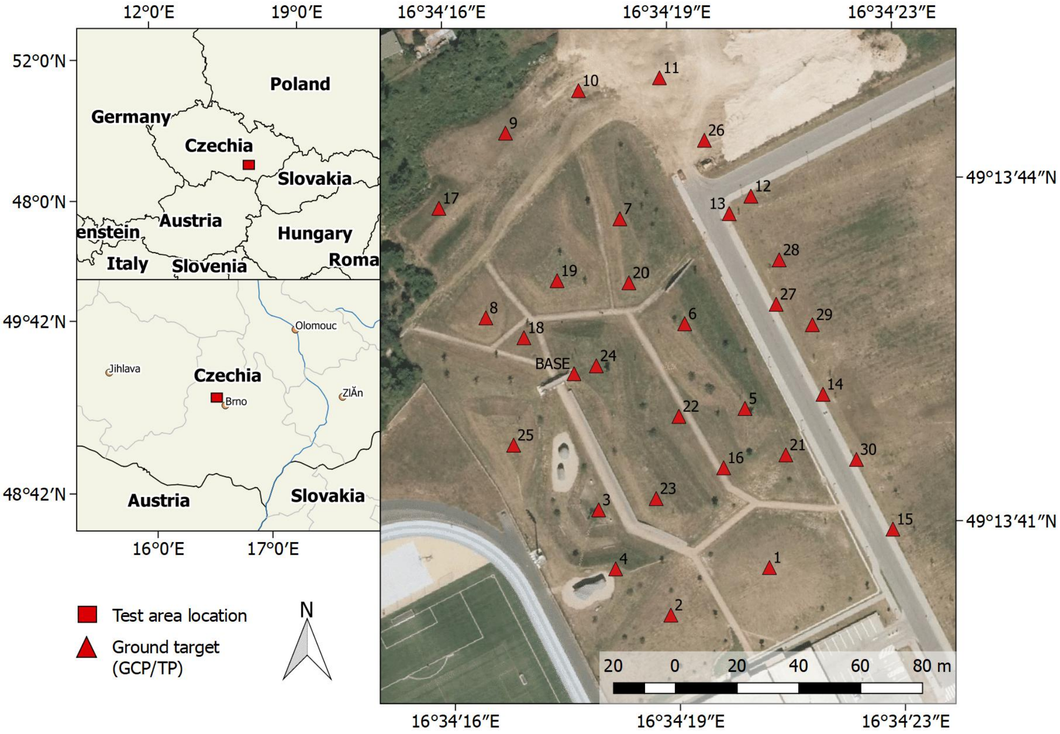

Figure 5. The test area and the distribution of the ground targets, which can be employed as GCPs or TPs (orthophoto adopted from CUZK (2010)).

enable accuracy assessment. We used 20 cm squared, black and white patterned paper targets having clearly defined centres (Figure 6(*a*)). Every target was glued onto a solid support and fixed to the ground using iron nails.

The position of every single target was obtained using a survey-grade Topcon HiPer Pro RTK GNSS receiver; this step was performed twice – before and after the flight. The device receives the correction data from CZEPOS (the provider of correction data from the Czech network of reference stations) via GSM; during the measurement, the receiver was stabilised with a tripod (Figure 6(*b*)). The position of the base station reference point (Section 2.4) was measured independently, using a Topcon GPT 3003N total station and a Topcon AT-G4 levelling instrument in the S-JTSK coordinate system (coordinates X, Y) and the Baltic Vertical Datum height system. After this measurement phase, adjustment was performed (coordinate h). The coordinates were transformed into the ETRS89 system via a local transformation key; the RMS error in the coordinates X, Y is 0.06 m. Figure 5 shows an ortophoto from the CUZK (The Administration of Land Surveying and Cadastre of Czech Republic) containing the coordinates of the ground targets and the base station.

2.7. *Aerial data acquisition*

The aerial data were acquired on 23 February 2017, together with the measurement of the ground targets. The weather allowed us to carry out the UAS flight and the photogrammetry measurement: it was overcast, 12 °C, with the wind of about 1–3 m s^{-1}. Since the UAS supports automatic flight according to GPS coordinates, the parameters of the flight trajectory and image acquisition were set before the flight.

(*a*) (*b*)

Figure 6. A detail of a ground target captured from the ground (*a*) and the process of the position measurement using survey-grade GNSS receiver (*b*). Location: 49°13'44.48"N, 16°34'16.14"E — WGS84.

Table 3. The parameters of the flight trajectory and image acquisition.

Parameter	**Symbol**[a]	**Value**
Distance between strips	A	20 m
Length of a strip	L	200 m
Number of a strips	-	7
Base (distance between consecutive images)	B	10 m
Flying altitude AGL	h	50 m
Flying speed	v	5 m s^{-1}
Time between images	t	2 s
Principal distance	c	15 mm
Photo scale	m_{b}	3333
Forward overlap	l	88 %
Side overlap	q	80 %
Footprint of image on the ground	-	120 × 80 m
Ground resolution	-	2 cm px^{-1}
Shutter speed	-	2000^{-1} s
Aperture	f	4.5
ISO	-	Auto (2,000–2,500)

[a] The symbols are based on Kraus (2007).

Several parameters are constant; thus, we have the sensor resolution of 6,000 × 4,000 px, focal length of 15 mm (Section 2.4), and the lowest possible safe AGL altitude of approximately 50 m. Under these conditions, the ground sample distance (GSD) corresponds to about 2 cm (or slightly more in lower-positioned locations).

The minimum forward and side overlaps for the object reconstruction are 50 % and 0 %, respectively; in practice, however, using a 60 % forward and a 30 % side overlap is recommended due to flight navigation inaccuracies (Kraus (2007)). Larger overlaps, such as those between 60 % and 90 %, are typically applied when precise surface reconstruction is needed (Turner, Lucieer, and Wallace (2014) and Rosnell and Honkavaara (2012)); however, the processing time increases dramatically (Torres-Snchez et al. (2017)). In our case, the camera was triggered every 2 seconds, and the flight speed equalled 5 m s^{-1}; such values should ensure the minimum forward overlap of 80 % for the whole test area. The flight trajectory contained 7 strips having the length of 200 meters and spacing of 20 meters. This configuration then led to 80 % side overlap. Table 3 summarises the flight trajectory parameters.

The flight lasted 8 minutes, enabling us to capture 194 images. The data from the INS were saved every time an image was taken, and the raw data from the GNSS receiver were saved continuously with the frequency of 50 Hz.

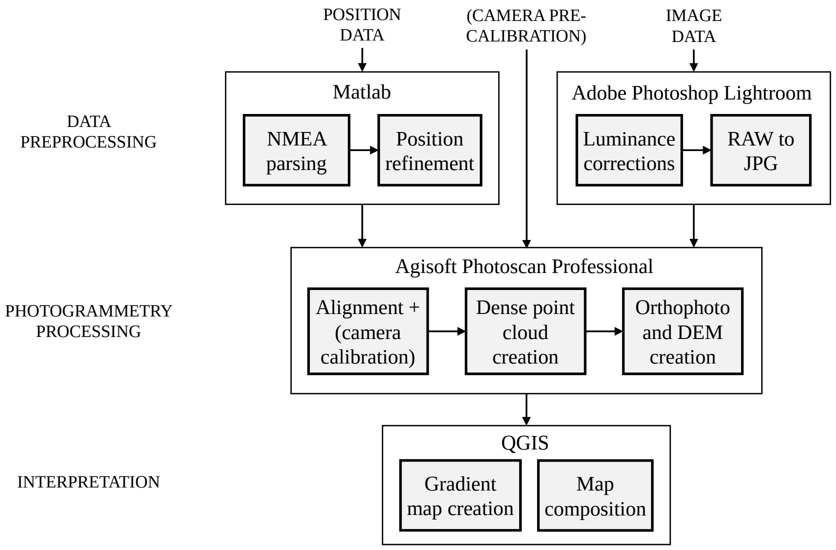

Figure 7. The sequence of the data processing operations.

2.8. *Data processing*

The present subsection describes the data processing workflow applied once the system calibration (Section 2.2), and possibly also camera pre-calibration (Section 2.3), has been performed. The calibrations provide the data enabling us to increase the accuracy of the exterior orientation measurement and photogrammetry processing.

Basically, there are two data types obtained during a photogrammetry mission, namely, GNSS/INS and image data. As the GNSS module receives the RTK correction data from the custom base station, the position is computed in real time. The INS fuses inertial and aiding data in real time too, and therefore no postprocessing is needed. The data parsing and conversion to an appropriate format, and also the position data refinement based on the proposed custom calibration (Section 2.2), are performed in Matlab. As regards the image data, we only apply some luminance transformations and subsequently convert the data from the RAW image format into the JPG format with minimal compression. The processing is illustrated in Figure 7.

For the photogrammetric processing, Agisoft Photoscan Professional v1.3.1 is used. This software was designed to facilitate surface reconstruction using digital image data, to generate georeferenced orthophotos and spatial models, and to support both direct and indirect georeferencing. The processing starts with the detection of feature points, which are matched across the whole image set. After filtering, the selected and matched tie points are used for the sparse point cloud creation, a process called structure-from-motion (SfM) (Verhoeven et al. (2012)). During this alignment stage, the interior and relative exterior orientations are also estimated. Within the following step, georeferencing can be performed via importing either the image position data measured by the onboard sensors or the positions of the GCPs obtained during ground measurement. This procedure exploits the similarity transformation already mentioned in Section 2.1. We should note in this context that the GNSS/INS data can be imported also before the align stage to speed up the processing.

Once the interior and exterior orientations of every image are known, the dense point cloud can be generated, utilizing multiview stereo reconstruction. As the operation is realised on pixel-level, we obtain a point cloud containing milions of points. Such a dense cloud then constitutes the basis for a true orthophoto, mesh, or DEM.

Photoscan allows us to use ground targets in two specific ways, namely, as GCPs for indirect georeferencing or as test/check points (TP/ChP) for an accuracy assessment. In both cases, the image position of the targets must be determined manually. If the imagery is georeferenced indirectly, some targets should be reserved as TPs. The influence exerted by the number and distribution of GCPs on ground accuracy is discussed in, for example, Vericat et al. (2009). Conversely, direct georeferencing facilitates using all available targets as TPs.

Photoscan is widely employed in scientific papers discussing aerial photogrammetry performed via manned and unmanned aircraft (Panayotov (2015), Turner, Lucieer, and Wallace (2014), Faraji, Qi, and Jensen (2016) etc.) because it implements state-of-the-art CV algorithms, ensures a clear workflow, offers multiple import and export options, and is reasonably priced.

3. Results

This section presents the achieved results; the accuracy of the ground and aerial data; the outcomes of the system calibration; and, finally, the object accuracy. In most cases, the results are expressed using root-mean-square error (RMSE), defined by (7), where x_i is the observed value, $\hat{x}_i$ the reference value, and N the number of observations.

$$\mathrm{RMSE} = \sqrt{\frac{1}{N}\sum_{i=1}^{N}(x_i - \hat{x}_i)^2} \tag{7}$$

A multi-dimensional RMS error RMSE_D is then computed according to (8), where D denotes the number of dimensions. This equation finds use in expressing the accuracy of the XY and XYZ positions.

$$\mathrm{RMSE}_D = \sqrt{\sum_{j=1}^{D}(\mathrm{RMSE})_j^2} \tag{8}$$

3.1. *Ground measurement*

As already mentioned in Section 2.6, the positions of the ground targets were measured before and after the flight, observing the delay of about 2 hours to ensure a different constellation of satellites. Such an approach is commonly practised to verify whether the data are consistent and whether an error did not affect one of the measurements.

As no reference measurement is performed, we can only compare the data with each other: $\boldsymbol{\Delta} = \boldsymbol{x}_{1,\mathrm{L}} - \boldsymbol{x}_{2,\mathrm{L}}$. The results indicate (Table 4) that the ground measurement is consistent and does not contain major deviations – the RMS error is approximately 1 cm in all axes. In the given respect, the Z axis exhibits the maximum error, one of about 4 cm; however, this is an isolated case, as clearly shown in Figure 8. Within the subsequent processing (GCPs and TPs), the averaged value of the measurements is used for every target.

Table 4. A comparison of the first and second measurements of ground targets.

Error type	X **(mm)**	Y **(mm)**	Z **(mm)**	XY **(mm)**	XYZ **(mm)**
RMS	5.2	10.4	12.8	11.7	17.3
Min (absolute)	0.7	0.3	1.0	1.4	4.1
Max (absolute)	10.4	22.6	39.0	23.1	39.8

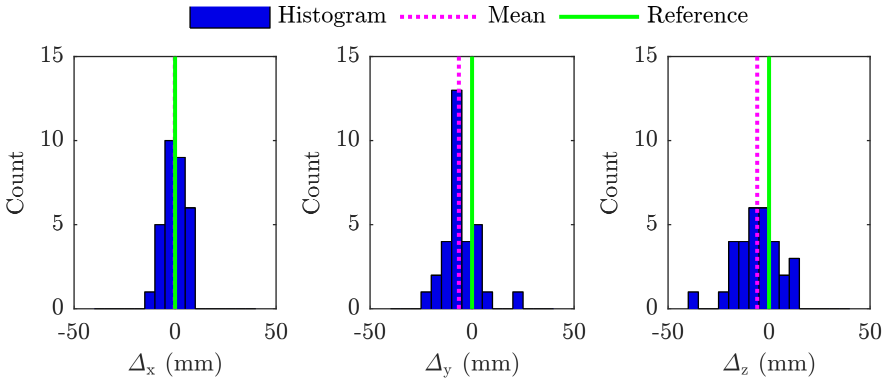

Figure 8. The histograms of errors between the first and second measurements.

3.2. *Flight and aerial data*

From the 194 images, only 137 were selected for processing. The images taken during the take-off and landing were manually selected and removed. Otherwise, this step can be carried out automatically since the coordinates of the start and end of the trajectory are known. The captured images, despite being perfectly sharp, are affected by a pair of significant issues due to the equipment used. Firstly, the wide angle lens mounted on the full frame camera caused the landing gear to be visible in all the images (Figure 9(a)); however, this is not a serious problem, because relevant portions of an image can be excluded from the processing by a constant mask. Secondly, we had to eliminate lens vignetting via compensation in Adobe Photoshop Lightroom. The RAW image files were then converted into JPG at minimum compression.

Although each photograph contains several targets, their image quality depends on the position in the given image. In the corners, above all, the geometric and brightness distortion deforms the targets, rendering them unsuitable for processing. Contrary to that, the targets found in the central portion of an image exhibit clearly recognizable centres; the size of the targets corresponds to $10 - 15$ pixels, as expected (Figure 9(b)).

The flight parameters described in Section 2.7 are theoretical and may vary slightly due to navigation inaccuracies and the low-accuracy GPS receiver incorporated in the flight control unit. This fact nevertheless should not affect the outcome of the experiment, because large overlaps are applied. The average flight speed measured by the GNSS/INS, excluding the take-off and landing phases, is 4.5 m s^{-1}. The average flight altitude above the starting point equals 46.3 m according to the GNSS/INS. As the starting point was situated at one of the highest locations within the area, the altitude AGL is more prominent in most of the zone.

The accuracy of the camera position measurement can be determined using aerial triangulation. To facilitate this step, Photoscan was employed for the indirect aerial imagery georeferencing, and all the 30 targets assumed the role of GCPs. During the

(*a*) (*b*)

Figure 9. The sample of one of the images from UAS after brightness transformation (*a*) and the detail of a target from the same image (*b*). Location: 49°13’41.61”N, 16°34’19.002”E — WGS84.

Table 5. The accuracy of the camera position measured by the onboard sensors before and after the custom calibration. The reference position is obtained from AT.

Calibration	Error type	X (mm)	Y (mm)	Z (mm)	XY (mm)	XYZ (mm)
No	Mean	-2.5	-38.2	8.7	157.4	158.9
	RMS	72.6	145.1	21.4	162.3	163.7
	Min (absolute)	7.1	1.4	0.3	79.1	94.3
	Max (absolute)	152.9	286.5	75.2	301.2	302.8
Yes	Mean	3.1	-19.4	8.7	37.0	43.0
	RMS	21.3	44.9	21.4	49.7	54.1
	Min (absolute)	0.1	0.1	0.3	2.5	3.8
	Max (absolute)	75.7	152.3	75.2	157.7	160.7

processing, the interior orientation of the camera was also estimated, and the set of parameters was exported as the reference camera calibration. The upper half of Table 5 presents the errors of the onboard position measurement compared to AT (Photoscan). The RMS errors of 162 mm for the horizontal position and 21 mm for the Z axis are rather unusual for a GNSS measurement: as a rule, horizontal accuracy is better than vertical. The non-standard condition probably arises from the synchronisation error between the INS measurement and the image capture moment, and this assumption is actually proven in Figure 10(*a*), where the horizontal error of all the camera positions is clearly in the direction of the flight.

3.3. *Calibration*

The custom calibration described in Section 2.2 uses the position data measured by the onboard sensors and obtained via AT to estimate the lever arm correction vector, synchronisation delay, and base station offset. Due to the nature of the flight trajectory, only the horizontal components of the vectors are estimated. A solution is found using the Gauss-Newton method, which estimates the unknowns iteratively to minimise the observation error (4). The vertical components of the lever arm and base station offset are correlated and cannot be separated during the estimation. The initial values for the lever arm correction and base station offset were chosen close to zero as the lever arm had been pre-calibrated and the base station offset is expected to be minimal. The initial value for the synchronisation delay was set to 0.01 second, according to the documentation of the INS unit and the camera parameters.

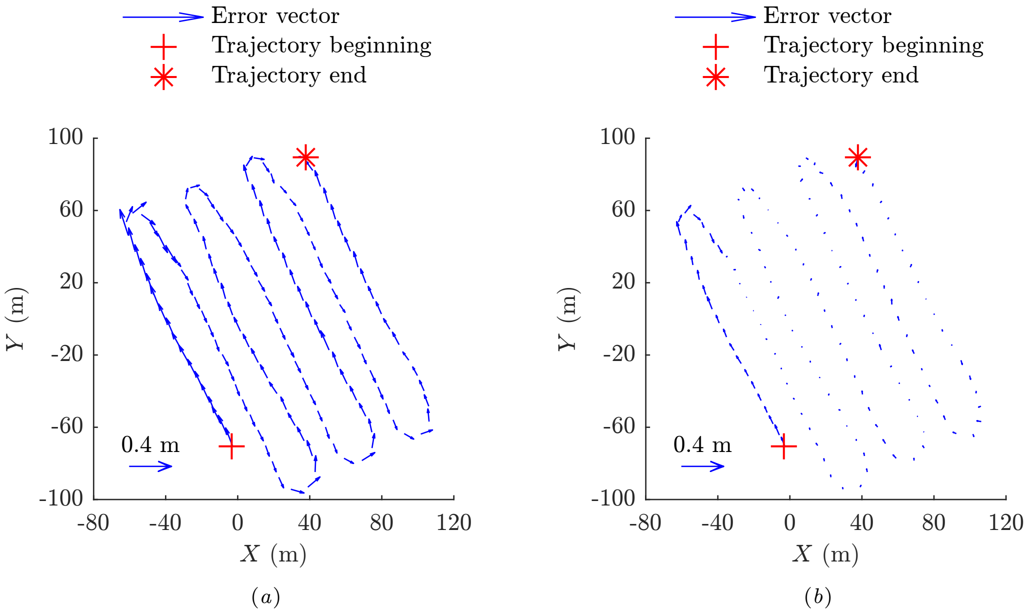

Figure 10. The camera position measurement error before (*a*) and after (*b*) the custom calibration. The arrows head from the AT (reference) position to the measured one, and they are 50x enlarged.

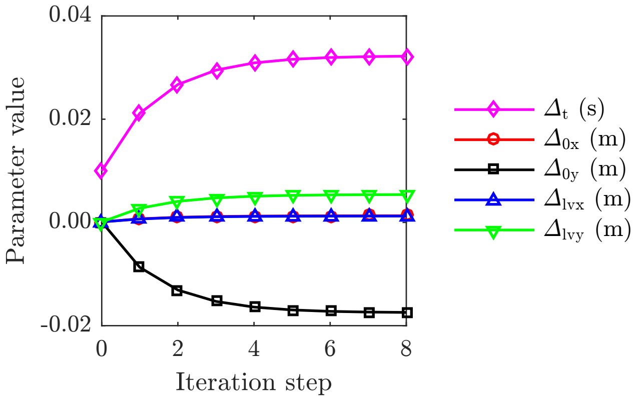

Figure 11. The value of the unknown parameters during the estimation process.

The five unknowns were obtained during 8 iteration steps, as illustrated in Figure 11. We found the following values of the unknowns: synchronisation delay $\varDelta_{\mathrm{t}} = 32.2$ ms; lever arm offset $(\varDelta_{\mathrm{lvx}}, \varDelta_{\mathrm{lvy}})$=(1.2, 5.4) mm; and base station offset $(\varDelta_{0\mathrm{x}}, \varDelta_{0\mathrm{y}})$=(1.3, -17.4) mm. These estimated parameters, excepting the base station offset, are ideally constant and can be used as the set of calibration parameters in future measurements. The parameters were employed to correct the measured position, which was again compared with the position obtained from AT. Table 5 shows that, after the calibration, the spatial RMS error decreased from 164 mm to 54 mm, producing an improvement of 67 %. With the sole exception of the trajectory origin (mainly the first strip), the error vectors are compensated, as demonstrated in Figure 10(*b*).

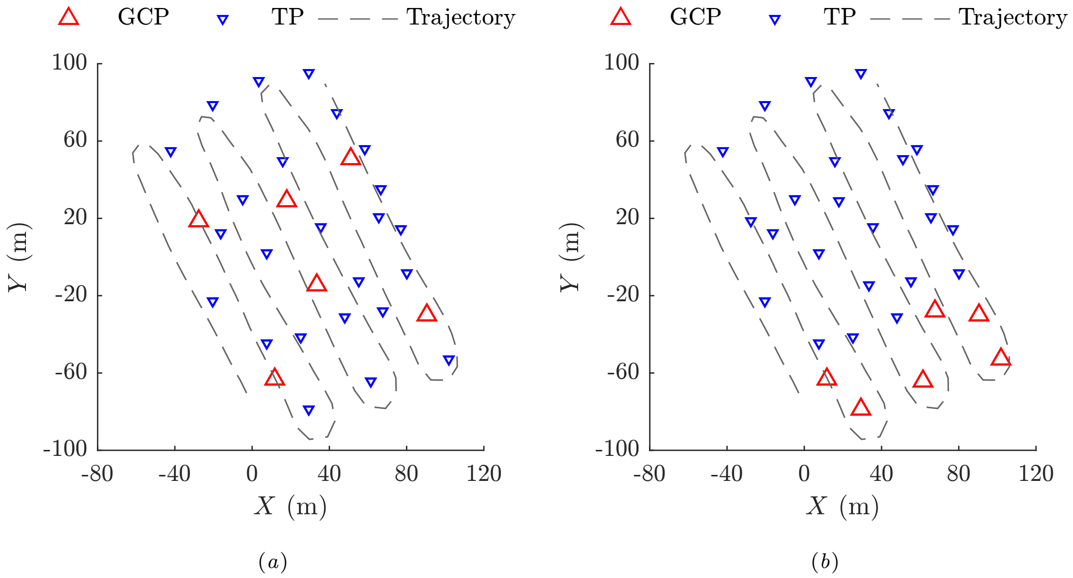

Figure 12. The distribution of the GCPs and TPs for the indirect georeferencing in versions #1a (*a*) and #1b (*b*).

3.4. *Object accuracy*

This section discusses the object point determination accuracy, namely, the accuracy of an orthophoto, point cloud, or another aerial photogrammetry product. The photogrammetric processing was invariably performed with Photoscan; in the georeferencing and calibration, however, different techniques were tested and compared. The accuracy was determined using ground targets, or test points, whose positions were measured by means of survey-grade equipment (Section 2.6). The results are summarised in Table 6, inspired by Cramer (2001), who studied a similar topic in the context of manned aircraft, and further illustrated in Figure 13.

First of all, we tested the accuracy of indirect georeferencing, the most common georeferencing technique in UAS photogrammetry. Version #1a in Table 6 presents the object accuracy of IG, where 6 well-distributed GPCs were used (Figure 12(*a*)), with the interior orientation parameters estimated during the photo alignment stage (field calibration). The RMS error did not exceed 1 cm for the X and Y and 2 cm for the Z coordinates (see Figures 14(*a*) and 14(*b*) for a graphical interpretation). The procedure was then repeated using another 6 GCPs, which, however were not distributed properly: all the GCPs lay in one part of the area, close to each other (Figure 12(*b*)). Such an arrangement corresponds to a situation where a portion of an area is inaccessible for some reason. The results indicate (version #1b) that the accuracy deteriorated, especially in the Z coordinate; at this axis, the RMS error increased almost five times, to 9 cm. The error is mostly systematic: the mean error corresponds about 7 cm. The interior orientation parameters can be pre-calibrated in a laboratory or during a calibration flight. Version #1c is nearly the same as #1a, the only difference consisting in that the interior orientation was not field-calibrated; instead, pre-calibrated parameters were used (Section 2.3). In terms of accuracy, this configuration performs significantly worse: the spatial RMS error increases by almost an order of magnitude, and the mean error dominates in the Z coordinate.

The second part of Table 6 introduces the results of the direct georeferencing pro-

Table 6. The object point determination accuracy acquired using different techniques and calibrations.

#	Configuration	GCP/ TP	Mean (mm) X	Y	Z	XY	XYZ	RMSE (mm) X	Y	Z	XY	XYZ
1a	IG well distr. *fc*	6/24	-3	-4	-6	5	8	9	9	20	12	24
1b	IG bad distr. *fc*	6/24	1	12	-72	12	73	7	19	92	20	94
1c	IG well distr. *pc*	6/24	-3	-3	-52	4	52	29	45	129	53	139
2a	DG-AT *fc*	0/30	2	33	-39	33	51	20	38	43	43	61
2b	DG-AT *pc*	0/30	-69	-89	429	113	444	159	197	439	253	507
2c	DG-AT *sc fc*	0/30	6	23	17	24	29	19	27	25	33	41
2d	DG-AT *sc pc*	0/30	-75	-115	458	137	478	178	229	471	290	553
3a	DG-AT + 1 GCP *sc fc*	1/29	7	10	14	12	18	18	17	22	25	33

Abbrev: *fc* – field-calibrated camera; *pc* – pre-calibrated camera; *sc* – system (custom) calibration.

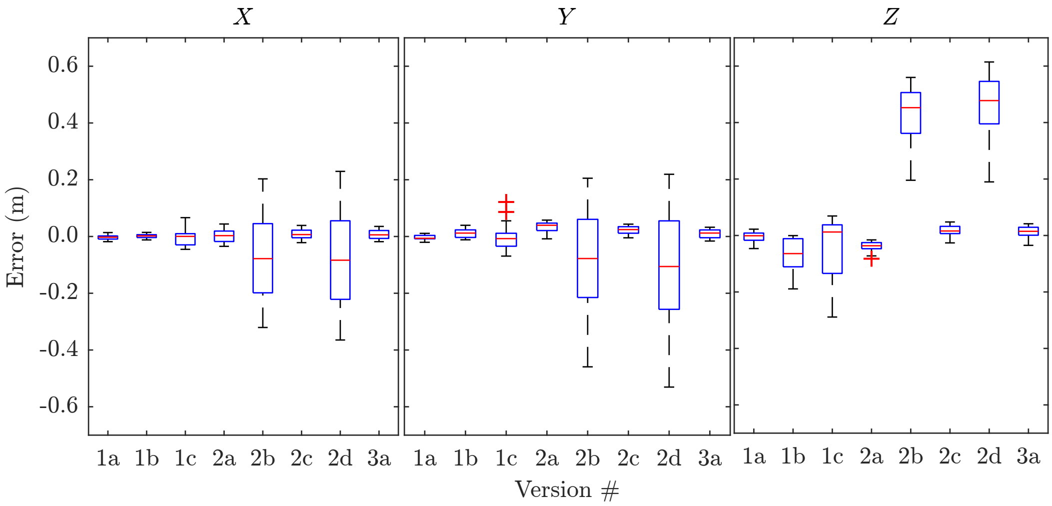

Figure 13. The object accuracy in all of the eight configurations.

cess, whose application embodies the central aim of the present paper. In the given context, DG denotes georeferencing without the use of GCPs and cannot be interpreted as *traditional* DG, because it is assisted by computer vision-based AT. The said traditional approach, which computes the object position directly through the use of the six exterior orientation elements measured by the onboard sensors, is not tested in this paper.

DG requires an accurate placement of sensors and time synchronisation. Version #2a results in a configuration where the lever arms between the GNSS antenna, INS unit, and camera were measured before the flight and saved into the INS unit; the time synchronisation is ensured by the hardware, as described in Section 2.4. During the photo alignment stage, the obtained position was refined, and the photogrammetric angles and interior orientation were estimated. The RMS error reached 2 cm for the X axis and about 4 cm for the Y and Z axes. The accuracy is 2 to 3 times worse compared to the IG in version #1a, and the mean error dominates. Once the pre-calibrated interior orientation parameters have been applied (version #2b), the accuracy decreased significantly. Both the mean and the RMS spatial errors increased

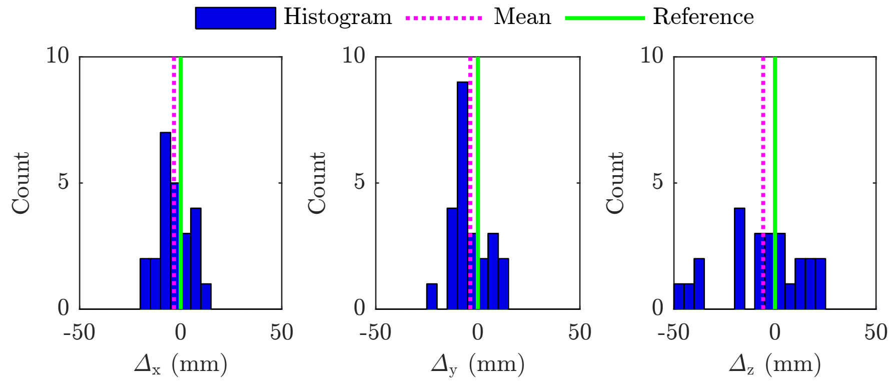

(*a*)

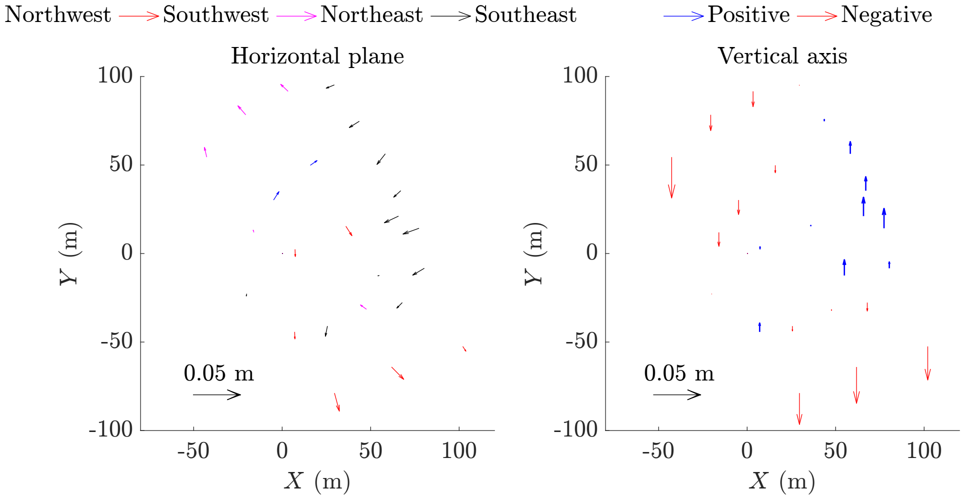

(*b*)

Figure 14. The object accuracy obtained via IG in version #1a. The histogram (*a*) shows the error distribution, and the plot (*b*) demonstrates the relationship between the error vectors and the test point positions (the vectors are enlarged 500 times).

by an order of magnitude.

In the previous chapters, we discussed a custom calibration procedure to estimate the synchronisation delay and lever arm offset. These parameters are constant and can be used for refining the measured data. Version #2c yields accuracy results acquired using custom calibration; contrary to #2a, #2c produced an improvement in all the axes, Y and Z in particular. After the custom calibration, the RMS error does not exceed 3 cm in all the axes (see Figures 15(*a*) and 15(*b*) for a graphical interpretation). The synchronisation delay compensation plays a major role here because it causes a position error depending on the speed and direction of the flight. When we supported the custom calibration with camera pre-calibration (version #2d), an accuracy decrease was observed, similarly to the previous cases.

The above-outlined results show that the field calibration of some constant parameters can increase the accuracy of DG; however, there are also certain systematic errors ineliminable without GCPs. This problem was already discussed by Cramer (2001), and it mainly consists in the offset of the position measurement performed by an onboard GNSS receiver and the inaccurate field calibration of camera interior param-

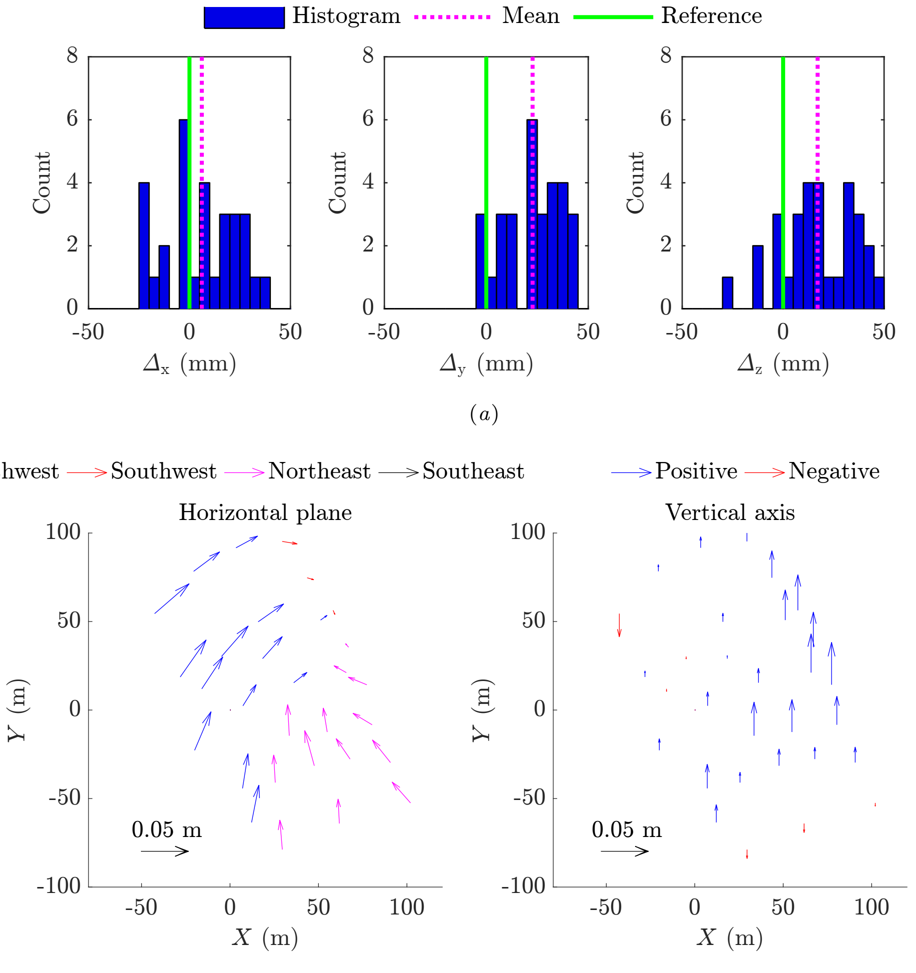

(a)

(b)

Figure 15. The object accuracy obtained via DG in version #2c. The histogram (*a*) shows the error distribution, and the plot (*b*) demonstrates the relationship between the error vectors and the test point positions (the vectors are enlarged 500 times).

eters. These systematic errors can be potentially compensated by a GCP. In version #3a, one GCP from the peripheral zone of the measured area (GCP #1, Figure 5) was used during the processing, together with the onboard GNSS/INS data. Each of the axes exhibits a slight improvement compared to version #2c, but the Y axis is prominent in this respect as the RMS error decreased by almost 1 cm. Since the mean error decreased too, the GNSS measurement shift was most probably compensated.

After the alignment stage, once the exterior orientation of all the images has been estimated, Photoscan can generate a georeferenced dense point cloud. Figure 16 displays a point cloud containing almost 29 million of points, which corresponds to a density of about 800 points m^{-2}. Based on this, an orthophoto, mesh, or DEM can be created.

Figure 16. A part of the georeferenced point cloud containing 29 million points. Location: 49°13'41.61"N, 16°34'19.002"E — WGS84.

4. Discussion

In this section, the results of the previous chapter are analyzed and compared with other current research papers. We also briefly discuss the perspectives of DG systems in micro- and light UASs.

4.1. *Positioning*

In order to assess the positioning accuracy of the designed multi-sensor system, we would need to possess reference data; however, as this category of UASs has very limited payload capabilities, it is not possible to carry another set of sensors providing better accuracy. The drawback can be eliminated via several suitable methods, and these are defined as follows: i) using a larger UAS or manned aircraft carrying a calibrated positioning system; ii) tracking the position of a UAS from the ground (presented in Blaha et al. (2012)); iii) utilizing AT to estimate the camera exterior orientation. We applied the last approach since 30 targets had already been distributed in the area. A comparison of the position data from AT and the GNSS/INS system showed a very clearly visible systematic error depending on the flight direction (Figure 10(a)). The proposed custom calibration then enabled us to establish that the error arises mainly from the synchronisation delay between the GNSS/INS and the camera shutter. The delay of 32 ms notably exceeds the expected value, and a closer look at the error vectors after the calibration (Figure 10(b)) will reveal a persisting systematic error in the flight direction at the beginning of the trajectory. This issue may arise from the fact that the delay was not constant throughout the flight; a step change in the delay could cause such behaviour. Another problem possibly rests in the estimation of the INS internal parameters: Ellipse-E INS utilises an extended Kalman filter to estimate the lever arms and angular misalignments between the GNSS and INS reference frames during an operation. Even though the parameters were initialised based on laboratory estimation, insufficient dynamics at the origin of the flight trajectory could cause their inaccurate estimation. The incorrect lever arm in the longitudinal axis might also produce the error visible in Figure 10(b). These assumptions are nevertheless still to be verified within future experiments. Regardless of this problem, the spatial positioning RMS error decreased by 67 % (to 54 mm) after the proposed system calibration.

The above-described practice shows that AT embodies a beneficial tool to evaluate the performance of DG systems and to calibrate them whenever no other reference data are available. As AT can estimate the full set of parameters related to the exterior orientation, a similar calibration technique can be used for evaluating and calibrating the angular elements (photogrammetric angles). However, the accuracy achievable with AT depends on the quality and distribution of the GCPs, as examined by, e.g., Vericat et al. (2009). The proposed calibration can nevertheless succeed only if certain flight parameters are met:

- The heading (azimuth) must not be constant throughout the flight; otherwise, the lever arm correction and the base station offset correlate and cannot be separated.
- The same condition applies to the lever arm correction and the synchronisation delay. These two parameters correlate perfectly and cannot be separated if the flight speed is constant, with the heading and course remaining mutually dependent throughout the flight.
- The synchronisation delay estimation presumes a linear flight trajectory and is thus applicable in small delays only.

4.2. *Georeferencing performance*

The previous section discussed positioning accuracy, an essential aspect of DG; object accuracy, however, depends also on the interior orientation and the performance of the CV methods implemented in the photogrammetric software used. Further, object accuracy can be evaluated directly, by being compared with ground measurement.

If we compare the object accuracies of the IG and DG used within the presented mission, then the IG clearly outperforms the other technique. The IG in version #1a reached the spatial RMS error of 2.4 cm, which is almost twice the accuracy of the DG in version #2c, namely, 4.1 cm. In both these cases, the interior orientation was field calibrated. Custom flight calibration proved to be very beneficial for the applied DG, yielding the improvement of 32 %; yet, at the same time, it should be noted that a major role is assumed here by the compensation of the synchronisation delay, which exceeded the originally expected value. The above two versions are also comparable using the graphical representation of errors in Figures 14 and 15. The character of the DG errors in Figure 15(b) is more systematic than that of the IG errors in Figure 14(b), meaning that some space still remains available for improving the proposed system.

Contrary to the custom system calibration, the interior orientation pre-calibration resulted in significant degradation of the object accuracy. In all of the pre-calibrated versions, the accuracy decreased by an order of magnitude. This observation shows that the lens interior parameters are not stable, mainly due to excessive clearances in the individual parts and mount of the camera. In our case, the camera field calibration allowed accurate interior orientation estimation according to the object accuracy assessment; the same outcomes are outlined in a relevant study by Harwin, Lucieer, and Osborn (2015).

The IG object accuracy presented in this paper (1.2 cm RMS for XY and 2.0 cm RMS for Z) is similar to the accuracies identified by Barry and Coakley (2013); Panayotov (2015); and Fazeli, Samadzadegan, and Dadrasjavan (2016) (see Section 1

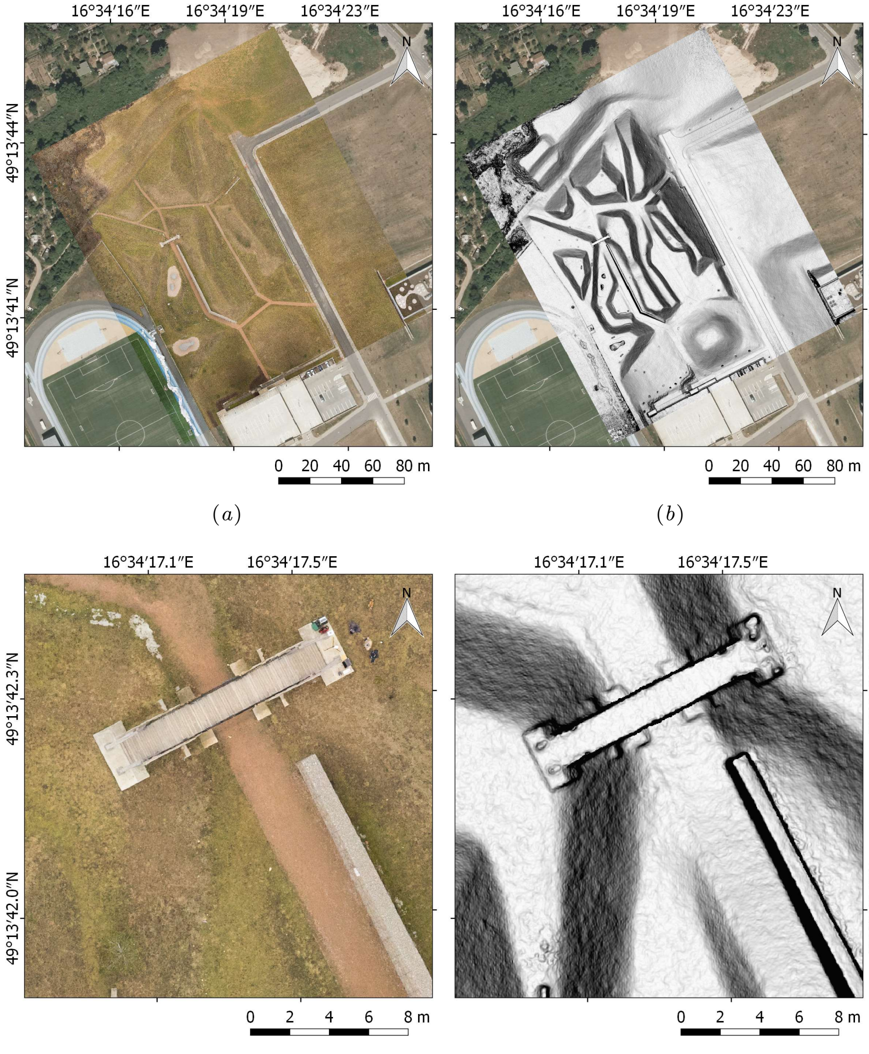

(*a*) (*b*)

(*c*) (*d*)

Figure 17. The ortophoto (*a*) and gradient map (*b*) created via the presented multi-sensor system as a layer over the orthophoto map adopted from CUZK (2010). Figures (*c*) and (*d*) show a detail of the bridge where the base station was located.

of the present article). If certain conditions are satisfied, the technique outlined herein ensures stable and predictable outcomes. From the perspective of georeferencing, the following items must be taken into account:

- The object accuracy directly depends on the accuracy of GCPs.
- Any inappropriate distribution of GCPs may negatively affect the object accuracy.

The established DG object accuracy (3.3 cm RMS for XY and 2.5 cm RMS for Z) appears to range among the top values achieved within the current research into the given problem. Such a result was obtained thanks to the state-of-the-art navigation and camera systems and the proposed custom calibration, which utilised complex data from the onboard sensors and AT to estimate the unknown parameters. Synchronisation delay estimation in particular is not common in today's implementations. More-over, the performance of our solution was determined thoroughly to produce credible outcomes. Comparable results are outlined by Eling et al. (2015), who employ a dual-antenna RTK-GNSS system carried by a multi-rotor UAS. Special attention is also paid to the time synchronisation and lever arm calibration. The object accuracy was tested during two flights; the first measurement yielded the RMS of 3.8 cm for XY and 3.0 cm for Z, and the second one resulted in 1.1 cm for XY and 0.9 cm for Z. Even though such outcomes are, in fact, very good, it should also be noted that the flight altitude (20 m) and speed (2 m s^{-1}) were low, and the performance of the second flight was verified on 9 test points only. The spatial accuracy of about 11 cm is presented by Turner, Lucieer, and Wallace (2014); their solution is nevertheless limited by a less accurate DGPS receiver. By comparison, Fazeli, Samadzadegan, and Dadrasjavan (2016) employed a low-cost RTK-GPS module, albeit only to also achieve the object accuracy at the decimetre level: 16.4 cm RMS for the XY and 23.5 cm for the Z axes. This is due to inaccurate time synchronisation and lever arm calibration.

In general, the accuracy of direct georeferencing is typically affected by the following factors:

- None or inaccurate lever arm calibration between the GNSS antenna and the camera perspective centre.
- Inaccurate time synchronisation between the onboard positioning system and the camera shutter.
- Inaccurate estimation of the interior orientation (camera parameters).

Traditional direct georeferencing, where the measured exterior orientation is directly used for the actual georeferencing, has become rather obsolete, especially in UAS photogrammetry. At present, specialised softwares estimate the photogrammetric angles and refine the measured positions, making attitude measurement redundant in the context of the application discussed herein. Figure 17 shows several outputs of the described mission: a directly georeferenced true orthophoto map with the ground resolution of about 2 cm px^{-1}, and a gradient map to illustrate the shape of the terrain.

4.3. *Outlook*

Although DG systems for micro- and light UASs do not match the accuracy of IG ones and are generally more challenging in terms of the calibration and equipment, they show a major potential for future use within diverse fields and disciplines. The advantage is obvious: the absence of GCPs saves a large amount of time and enables fully automated data processing. These systems have expanded primarily due to the decreasing cost and size of accurate INS and RTK-GNSS systems. In recent years, such UAS systems for DG have begun to appear on the market. For example, senseFly (senseFly (2017)) offers a UAS equipped with an RTK-GNSS receiver designed for DG with the object accuracy of 3 cm at each axis (according to the specification). This fixed-wing UAS is capable of flying for almost 1 hour, thus covering several square kilometres; the independence from GCPs is then highly beneficial. Such UASs are typically not as sophisticated as the solution proposed within this paper, which exploits the leading navigation system technologies. A case study presented on 3DroneMapping (2016) shows that a centimetre-level object accuracy can also be reached using much simpler equipment, namely, a fixed-wing UAS fitted with a single-antenna single-frequency GNSS receiver supporting post processed kinematic (PPK); the UAS does not comprise a dedicated INS unit. In all the cases, however, it is good practice to use some test points for the accuracy assessment and quality assurance.

5. Conclusion

This paper presents a custom-built system for the direct georeferencing of aerial imagery, designed specially for micro- and light UASs. The related multi-sensor system was implemented and successfully tested during several missions; one of the experiments is described in detail herein. To achieve high accuracy, we employed leading navigation system technologies, namely, an RTK-GNSS receiver and an INS unit to fuse the positioning and inertial data. The proposed field calibration method enables the system to attain centimetre-level object accuracy without the need of ground control points.

A significant portion of the research consisted in assessing the accuracy of the whole system; for that reason, 30 test points were deployed within the test area. The performance of the direct and the indirect georeferencing methods and different calibration techniques was examined. The applied direct georeferencing, supported by the proposed field calibration, yielded the spatial object accuracy of 4.1 cm RMS, which is an improvement of 32 % compared to the accuracy without the calibration. The object accuracy of 2.4 cm RMS was achieved via the indirect georeferencing method, using 6 test points as GCPs. The results indicate that IG can be very accurate even with a consumer-grade camera and no additional onboard sensors. However, the introduced DG object accuracy is sufficient for most applications, and the fact that ground measurement is not necessary constitutes a highly beneficial aspect.

The presented multi-sensor system for UASs finds use in fields where GCPs cannot be utilised. Such a situation usually occurs in areas inaccessible or dangerous to humans, including zones of natural disasters, radiation hotspot localisation, or environmental mapping. The system was successfully employed in a gamma radiation mapping experiment which examined the potential of cooperation between UAS and UGV during the localisation of hotspots; the outcomes are presented in Lazna et al. (2018) and Lazna et al. (2017).

Funding

This work was supported by the European Regional Development Fund under the project Robotics for Industry 4.0 (reg. no. CZ.02.1.01/0.0/0.0/15_003/0000470) and by the Technology Agency of the Czech Republic under the project TE01020197 ”Centre for Applied Cybernetics 3”.

References

3DroneMapping. 2016. “3DroneMapping completes PPK trials.” Accessed 2017-07-31. `https://3dronemapping.com/3dronemapping-completes-ppk-trials/`.

Agisoft. 2017. “Agisoft PhotoScan User Manual: Professional Edition, Version 1.3.” `http://www.agisoft.com/pdf/photoscan-pro_1_3_en.pdf`.

Arjomandi, Maziar, Shane Agostino, Matthew Mammone, Matthieu Nelson, and Tong Zhou. 2006. “Classification of Unmanned Aerial Vehicles.” `http://afrsweb.usda.gov/SP2UserFiles/Place/62351500/Unmanned.pdf`.

Barry, P., and R. Coakley. 2013. "Field Accuracy Test of RPAS Photogrammetry." *ISPRS - International Archives of the Photogrammetry, Remote Sensing and Spatial Information Sciences* XL-1/W2: 27–31. Accessed 2016-08-02. `http://www.int-arch-photogramm-remote-sens-spatial-inf-sci.net/XL-1-W2/27/2013/`.

Blaha, M., H. Eisenbeiss, D. Grimm, and P. Limpach. 2012. "Direct Georeferencing of UAVs." *ISPRS - International Archives of the Photogrammetry, Remote Sensing and Spatial Information Sciences* XXXVIII-1/C22: 131–136. Accessed 2014-04-17. `http://www.int-arch-photogramm-remote-sens-spatial-inf-sci.net/XXXVIII-1-C22/131/2011/isprsarchives-XXXVIII-1-C22-131-2011.html`.

Brown, Duane C. 1966. "Decentering Distortion of Lenses." *Photogrammetric Engineering* 32 (3): 444–462.

Brown, Duane C. 1971. "Close-range camera calibration." *Photogrammetric Engineering* 37 (8): 855–866.

Cramer, Michael. 2001. "Performance of GPS/Inertial Solutions in Photogrammetry." .

CUZK. 2010. "CUZK - Geoportal." Accessed 2017-03-15. `http://geoportal.cuzk.cz`.

Deuflhard, Peter. 2011. "Least Squares Problems: Gauss-Newton Methods." In *Newton Methods for Nonlinear Problems*, Springer Series in Computational Mathematics, 173–231. Springer, Berlin, Heidelberg. DOI: 10.1007/978-3-642-23899-4_4, Accessed 2017-12-22. `https://link.springer.com/chapter/10.1007/978-3-642-23899-4_4`.

Eling, C., M. Wieland, C. Hess, L. Klingbeil, and H. Kuhlmann. 2015. "Development and Evaluation of a UAV Based Mapping System for Remote Sensing and Surveying Applications." *ISPRS - International Archives of the Photogrammetry, Remote Sensing and Spatial Information Sciences* XL-1/W4: 233–239. Accessed 2016-08-03. `http://www.int-arch-photogramm-remote-sens-spatial-inf-sci.net/XL-1-W4/233/2015/`.

Elsharkawy, Ahmed S., and Ayman F. Habib. 2016. "Error Analysis for the Airborne Direct Georeferincing Technique." *ISPRS - International Archives of the Photogrammetry, Remote Sensing and Spatial Information Sciences* 41B1: 1213–1219. Accessed 2018-01-03. `http://adsabs.harvard.edu/abs/2016ISPAr41B1.1213E`.

Faraji, Mohammad Reza, Xiaojun Qi, and Austin Jensen. 2016. "Computer visionbased orthorectification and georeferencing of aerial image sets." *Journal of Applied Remote Sensing* 10 (3): 036027–036027. Accessed 2017-05-25. `http://dx.doi.org/10.1117/1.JRS.10.036027`.

Fazeli, H., F. Samadzadegan, and F. Dadrasjavan. 2016. "Evaluating the Potential of RTK-UAV for Automatic Point Cloud Generation in 3D Rapid Mapping." In *ISPRS - International Archives of the Photogrammetry, Remote Sensing and Spatial Information Sciences*, Vol. XLI-B6, Jun., 221–226. Copernicus GmbH. Accessed 2017-05-25. `http://www.int-arch-photogramm-remote-sens-spatial-inf-sci.net/XLI-B6/221/2016/`.

Gabrlik, Petr, Ales Jelinek, and Premysl Janata. 2016. "Precise Multi-Sensor Georeferencing System for Micro UAVs." In *IFAC-PapersOnLine*, Vol. 49, Brno, Czech Republic, 170–175. Elsevier Ltd. Accessed 2017-03-13. `http://www.sciencedirect.com/science/article/pii/S2405896316326659`.

Han, Soohee, Jinhwan Park, and Wonhee Lee. 2016. "On-Site vs. Laboratorial Implementation of Camera Self-Calibration for UAV Photogrammetry." *Journal of the Korean Society of Surveying, Geodesy, Photogrammetry and Cartography* 34 (4): 349–356. DOI: 10.7848/ksgpc.2016.34.4.349.

Hartley, Richard, and Andrew Zisserman. 2004. *Multiple View Geometry in Computer Vision*. 2nd ed. Cambridge University Press.

Harwin, Steve, Arko Lucieer, and Jon Osborn. 2015. "The Impact of the Calibration Method on the Accuracy of Point Clouds Derived Using Unmanned Aerial Vehicle Multi-View Stereopsis." *Remote Sensing* 7 (9): 11933–11953. Accessed 2017-11-20. `http://www.mdpi.com/2072-4292/7/9/11933`.

Jilek, T. 2015. "Radiation intensity mapping in outdoor environments using a mobile robot with RTK GNSS." In *International Conference on Military Technologies (ICMT) 2015*, May, 1–7.

Kocmanova, Petra, and Ludek Zalud. 2015. "Multispectral Stereoscopic Robotic Head Calibration and Evaluation." In *Modelling and Simulation for Autonomous Systems*, Lecture Notes in Computer Science, Apr., 173–184. Springer, Cham. Accessed 2017-08-16. `https://link.springer.com/chapter/10.1007/978-3-319-22383-4_13`.

Kraus, Karl. 2007. *Photogrammetry: Geometry from Images and Laser Scans.* Walter de Gruyter.

Lari, Z., and N. El-Sheimy. 2015. "System Considerations and Challendes in 3d Mapping and Modeling Using Low-Cost Uav Systems." *ISPRS - International Archives of the Photogrammetry, Remote Sensing and Spatial Information Sciences* 3: 343–348. Accessed 2018-01-03. `http://adsabs.harvard.edu/abs/2015ISPAr.XL3..343L`.

Lazna, Tomas, Petr Gabrlik, Tomas Jilek, and Ludek Zalud. 2018. "Cooperation between an unmanned aerial vehicle and an unmanned ground vehicle in highly accurate localization of gamma radiation hotspots." *International Journal of Advanced Robotic Systems* 15 (1): 1–16. Accessed 2018-01-08. `https://doi.org/10.1177/1729881417750787`.

Lazna, Tomas, Tomas Jilek, Petr Gabrlik, and Ludek Zalud. 2017. "Multi-robotic area exploration for environmental protection." In *Lecture Notes in Computer Science*, Vol. 10444, Lyon, France, Jan., 240–254. Springer, Cham. `https://link.springer.com/chapter/10.1007/978-3-319-64635-0_18`.

Lo, C. F., M. L. Tsai, K. W. Chiang, C. H. Chu, G. J. Tsai, C. K. Cheng, N. El-Sheimy, and H. Ayman. 2015. "The Direct Georeferencing Application and Performance Analysis of Uav Helicopter in Gcp-Free Area." In *The International Archives of Photogrammetry, Remote Sensing and Spatial Information Sciences; Gottingen*, Vol. XL, Gottingen, Germany, 151–157. Copernicus GmbH. Accessed 2017-11-29. `https://search.proquest.com/docview/1756968633/abstract/B238140DB5964263PQ/1`.

Panayotov, Apostol. 2015. "Photogrammetric Accuracy of Real Time Kinematic Enabled Unmanned Aerial Vehicle Systems." Oct. `http://uas.usgs.gov/pdf/Reports/USGS_FINAL_REPORT_10212015.pdf`.

Pfeifer, N., P. Glira, and C. Briese. 2012. "Direct Georeferencing with on Board Navigation Components of Light Weight Uav Platforms." *ISPRS - International Archives of the Photogrammetry, Remote Sensing and Spatial Information Sciences* 39B7: 487–492. Accessed 2018-01-03. `http://adsabs.harvard.edu/abs/2012ISPAr39B7..487P`.

Rehak, M., R. Mabillard, and J. Skaloud. 2013. "A micro-UAV with the capability of direct georeferencing." Vol. 40, 317–323.

Rieke, M., T. Foerster, J. Geipel, and T. Prinz. 2012. "High-precision Positioning and Real-time Data Processing of UAV-Systems." *ISPRS - International Archives of the Photogrammetry, Remote Sensing and Spatial Information Sciences* XXXVIII-1/C22: 119–124. Accessed 2016-07-26. `http://www.int-arch-photogramm-remote-sens-spatial-inf-sci.net/XXXVIII-1-C22/119/2011/`.

Rosnell, Tomi, and Eija Honkavaara. 2012. "Point Cloud Generation from Aerial Image Data Acquired by a Quadrocopter Type Micro Unmanned Aerial Vehicle and a Digital Still Camera." *Sensors* 12 (1): 453–480. Accessed 2015-09-28. `http://www.mdpi.com/1424-8220/12/1/453`.

Sakr, M., Z. Lari, and N. El-Sheimy. 2016. "Design and Implementation of a Low-Cost Uav-Based Multi-Sensor Payload for Rapid-Response Mapping Applications." *ISPRS - International Archives of the Photogrammetry, Remote Sensing and Spatial Information Sciences* 41B1: 1017–1022. Accessed 2018-01-03. `http://adsabs.harvard.edu/abs/2016ISPAr41B1.1017S`.

senseFly. 2017. "eBee Plus." Accessed 2017-07-31. `https://www.sensefly.com/drones/ebee-plus.html`.

Torres-Snchez, Jorge, Francisca Lpez-Granados, Irene Borra-Serrano, and Jos Manuel Pea. 2017. "Assessing UAV-collected image overlap influence on computation time and digital surface model accuracy in olive orchards." *Precision Agriculture* 1–19. Accessed 2017-12-20. `https://link.springer.com/article/10.1007/s11119-017-9502-0`.

Turner, D., A. Lucieer, and L. Wallace. 2014. "Direct Georeferencing of Ultrahigh-Resolution

UAV Imagery." *IEEE Transactions on Geoscience and Remote Sensing* 52 (5): 2738–2745.

Verhoeven, G., M. Doneus, Ch. Briese, and F. Vermeulen. 2012. "Mapping by matching: a computer vision-based approach to fast and accurate georeferencing of archaeological aerial photographs." *Journal of Archaeological Science* 39 (7): 2060–2070. Accessed 2016-03-08. `http://www.sciencedirect.com/science/article/pii/S0305440312000866`.

Vericat, Dami, James Brasington, Joe Wheaton, and Michaela Cowie. 2009. "Accuracy assessment of aerial photographs acquired using lighter-than-air blimps: low-cost tools for mapping river corridors." *River Research and Applications* 25 (8): 985–1000. `http://onlinelibrary.wiley.com/doi/10.1002/rra.1198/abstract`.

Zalud, Ludek, Petra Kocmanova, Frantisek Burian, Tomas Jilek, Petr Kalvoda, and Lukas Kopecny. 2015. "Calibration and Evaluation of Parameters in A 3D Proximity Rotating Scanner." *Elektronika Ir Elektrotechnika* 21 (1): 3–12. WOS:000349838500001.